



# High ampacity of superhelix graphene/copper nanocomposite wires by a synergistic growth-twisting-drawing strategy

Kai Zhao <sup>a, b</sup>, Tengfei Zhang <sup>a, b</sup>, Ai Ren <sup>a, b</sup>, Yang Yang <sup>a, b</sup>, Peishuang Xiao <sup>a, b</sup>, Zhen Ge <sup>a, b</sup>, Yanfeng Ma <sup>a, b</sup>, Yongsheng Chen <sup>a, b, \*</sup>

<sup>a</sup> State Key Laboratory of Elemento-Organic Chemistry, Centre of Nanoscale Science and Technology and Key Laboratory of Functional Polymer Materials, College of Chemistry, Nankai University, Tianjin, 300071, China

<sup>b</sup> Collaborative Innovation Center of Chemical Science and Engineering (Tianjin), Tianjin, 300071, China



## ARTICLE INFO

### Article history:

Received 25 June 2018

Received in revised form

10 September 2018

Accepted 11 September 2018

Available online 12 September 2018

## ABSTRACT

Nanocarbon materials can provide effective reinforcement to a surrounding composite matrix. However, the fabrication of nanocarbon/metal composites with superior comprehensive properties remains challenging. Here, we developed a simple cyclic growth-twisting-drawing method to fabricate superhelix graphene/copper nanocomposite wires composed of massive, strongly bonded, and super-helically arranged fine copper fibers with interfacial graphene layers. The obtained nanocomposite wires with a small graphene volume fraction of ~0.32% exhibit a largely improved current carrying capacity of  $5.8 \times 10^{10} \text{ A m}^{-2}$ , ~2.6 times of that of pure copper wires. Furthermore, the electrical conductivity,  $5.01 \times 10^7 \text{ S m}^{-1}$ , is comparable to that of pure copper. These nanocomposite wires also exhibit improved strength and ductility, 10% and 80% increases compared with that of pure copper wires. These multiple enhanced properties can be attributed to the microscopic superhelix structure with the interfacial graphene layers embedded in the entire multi-level structure. With their largely improved current carrying capacity and mechanical reinforcement, these highly electrically conductive nanocomposite wires promise widely potential applications in the areas of heavy duty, high power electronics and electricity transmission.

© 2018 Elsevier Ltd. All rights reserved.

## 1. Introduction

Highly electrically conductive materials with supreme current carrying capability (ampacity) are emerging to meet the demand for both the tremendous expansion of electric power systems and the progressive miniaturization of micro electronic devices [1,2]. On one hand, the ampacity is intrinsically determined by electromigration, a nonthermal and current-assisted diffusion process initiated at surface and grain boundaries [3,4]. On the other hand, a series of complexities, including joule-heating-induced temperature rise, surface emissivity, heat dissipation coefficients, as well as neighboring heat sources, all impact the restricted current in practical applications [2,5,6]. Traditional metal conductors, such as copper (Cu) and aluminum (Al), are widely used in electrical

applications such as wires and cables due to their outstanding electrical conductivity. However, the current limit by electromigration is approximately  $10^{10} \text{ A m}^{-2}$  in most metals, generally two orders of magnitude lower than that of nanocarbons ( $\sim 10^{12} \text{ A m}^{-2}$ ) [7–10]. Moreover, their limited melting point and thermal/chemical stability as compared to that of carbon-based materials, for example graphite conductors, hinders their applications under heavy-duty and high-power conditions, as well as harsh environments. In contrast, nanocarbons such as graphene and carbon nanotubes (CNTs) are characterized by their remarkable ability to sustain high current density, as well as their ultra-high thermal and chemical stability [11,12] due to strong C–C bonds. However, the low electrical conductivity of nanocarbons and their macroscopic assemblies are still obstacles when used as conductors [8,13]. Generally, high ampacity and high conductivity are mutually exclusive properties. This is because the former requires a strongly bonded system, whereas the latter requires the free electrons from a weakly bonded one [1,14]. Therefore, achieving high electrical conductivity and ampacity, as well as thermal and mechanical

\* Corresponding author. State Key Laboratory of Elemento-Organic Chemistry, Centre of Nanoscale Science and Technology and Key Laboratory of Functional Polymer Materials, College of Chemistry, Nankai University, Tianjin, 300071, China.  
E-mail address: [yschen99@nankai.edu.cn](mailto:yschen99@nankai.edu.cn) (Y. Chen).

stability, in a single material is still great challenge.

Recently, graphene- and CNTs-based fibers and wires were developed for high performance electrical cables with high ampacity [12,15–17]. However, their intrinsic low electrical conductivity is still a problem. Owing to their unique structure and excellent properties, nanocarbons can serve as property enhancer for composite materials to achieve comprehensive properties [18–20]. Especially, graphene/metal and CNTs/metal composites synergistically combine the high electrical conductivity of metals and the high ampacity of nanocarbons [1,17,21]. But the alignment and distribution with increasing volume fraction of nanocarbon inclusions remains challenging, which limits the maximum reinforcement. More recently, nanolayered structures, such as graphene/polymer and graphene/metal nanolayered composite materials [22–26], are reported to have high degrees of enhancement due to uniform distribution, high alignment and high-quality of chemical vapor deposition (CVD) graphene, as well as considerably reduced interface spacing. Nevertheless, such fabrication processes are difficult to apply for fabricating fibers and wires. As a result, there is high demand for better methods to fabricate nanocarbon/metal composite wires or fibers with largely improved comprehensive properties.

In this study, we fabricated graphene/Cu nanocomposite wires through a synergistic growth-twisting-drawing strategy, which is a unique cyclic three-step process including (1) growth of surface graphene by CVD, (2) twisting of the graphene coated wires, and (3) densification of the twisted wires by multi-die drawing. The CVD produces high quality graphene crystals in situ and ensures sufficient interaction between the graphene sheets and the copper crystal domains at microscopic scale. The repeated twisting-drawing processes make the graphene finally to be closely spaced but distinctly separated, and distributed highly uniformly within the copper matrix. The obtained graphene/Cu nanocomposite wires possess a superhelix micro texture (superhelix G@Cu wires), that is a bundle of massive, strongly bonded and super-helically arranged fine Cu fibers interpenetrated by almost continuous and high quality interfacial graphene layers. Compared to commercial Cu wires, the superhelix G@Cu wires exhibit largely improved ampacity, enhanced strength and ductility, and almost unchanged electrical and thermal conductivity. These superior comprehensive properties can be attributed to the unique superhelix structure, together with the nano-confinement effect and excellent properties of graphene.

## 2. Experimental methods

### 2.1. Fabrication of graphene coated Cu wires (G/Cu wires)

Graphene coated Cu wires were fabricated by a modified CVD method based on a well-established procedure reported elsewhere [27]. Commercial Cu wires (diameter of 200  $\mu\text{m}$ ) that fixed separately on quartz holders were placed in a modified vertical tubular furnace (Tianjin Zhonghuan Lab Furnace Co., Ltd). After annealing at 1000 °C under Ar/H<sub>2</sub> atmosphere (200 sccm Ar and 50 sccm H<sub>2</sub> flows) for 40 min, the CVD growth of graphene was carried out at 1000 °C by adding 5 sccm methane for 20 min, followed by furnace cooling under Ar/H<sub>2</sub> atmosphere (200 sccm Ar and 50 sccm H<sub>2</sub>). The obtained samples of graphene coated Cu wires were named G/Cu wires.

### 2.2. Fabrication of superhelix graphene/Cu nanocomposite wires (superhelix G@Cu wires)

6 of as prepared G/Cu wires were twisted and then subjected to 5–6 times of a repeating two-step treatment including pre-tension

below 100 °C and then 1000 °C annealing for 30 min under Ar/H<sub>2</sub> atmosphere (200 sccm Ar and 50 sccm H<sub>2</sub>) using the CVD furnace. At this stage, the samples were named G/Cu-T wires. Subsequently, the G/Cu-T wires were drawn through a series of circular dies (decreased hole diameters from 570 to 200  $\mu\text{m}$ , 30  $\mu\text{m}$  in step,  $\sim 100 \text{ mm min}^{-1}$ ) manually at room temperature (RT), which produced samples named 1st superhelix G@Cu wires. Again, the CVD process was carried out with the 1st superhelix G@Cu wires after the multi-die drawing treatment, and the obtained samples were used for the next fabrication cycle. The above growth-twisting-drawing procedure was cycled for  $n$  times to produce superhelix graphene/Cu nanocomposite wires named  $n$ th superhelix G@Cu wires ( $n = 1-6$ ). In addition, control samples ( $n$ th superhelix Cu wires,  $n = 1-6$ ) were fabricated from commercial Cu wires without surface graphene and following the similar procedures above without CVD growth.

### 2.3. Morphology and structural characterization

The microscopic morphologies of the samples were observed by a field emission scanning electron microscopy (FE-SEM, Model S-4300, Hitachi, Japan) equipped with an energy-dispersive X-ray spectrometry (EDS) system. Secondary electron SEM images were taken for both the axial surface and radial cross-section with an acceleration voltage of 15–20 kV. The cross-section of the G/Cu wires and  $n$ th superhelix G@Cu wires were obtained by tensile fracture at a displacement rate of 1  $\text{mm min}^{-1}$  using an electronic universal testing machine (Shimadzu, AG-X), and by manually cutting using a scalpel for the G/Cu-T wires. Carbon elements distribution beneath the axial surface of the  $n$ th G@Cu wires were investigated by the EDS measurements, where the samples were mechanically polished to eliminate the surface graphene and then partially etched in ferric chloride (FeCl<sub>3</sub>) aqueous solution (0.5  $\text{mol L}^{-1}$ ) followed by thorough cleaning.

Both the surface and interior graphene was assessed by Raman spectrometry (Renishaw, inVia Raman spectrometer) with a wavelength of 514 nm. For the Raman examination of the interior graphene, two types of samples were prepared and measured as follows. Using the dip cast method, polymethyl methacrylate (PMMA) coatings were deposited from its chloroform solution (40  $\text{mg mL}^{-1}$ ) to the outer surface of the commercial Cu wires and surface-polished  $n$ th superhelix G@Cu wires, respectively. Subsequently, Cu was totally etched in the FeCl<sub>3</sub> aqueous solution (0.5  $\text{mol L}^{-1}$ ) followed by thorough cleaning to leave the PMMA coatings. In the case of the surface-polished  $n$ th G@Cu wires, the measured PMMA coatings should adhere with residual graphene sheets that originally in the interior of the nanocomposite wires. The PMMA coatings obtained from the commercial Cu wires were then measured to distinguish the PMMA background.

### 2.4. Density measurements

All the measured samples were cut into a length ( $L$ ) of 5 mm. The mean diameter ( $d$ ) was measured by SEM mentioned above. The mass ( $m$ ) was measured using a balance with a precision of 0.1 mg (Sartorius, BSA124S-CS). The mass density ( $\rho$ ) was calculated using the expression:  $\rho = 4 \times m / (L \times \pi \times d \times d)$ . The standard errors were calculated from three measured samples for each type of the wires.

### 2.5. Measurements of mechanical properties

Monotonic tensile tests were performed using an electronic universal testing machine (Shimadzu, AG-X) with a precision of 0.1 mN and 0.033  $\mu\text{m}$ . All the samples were fixed by glue between the two counter holders with a tested gauge length of 15 mm. The

displacement rate was set to  $1 \text{ mm min}^{-1}$ . True stress-strain curves were obtained using a constant-volume, homogenous deformation model [25,28]. The Young's modulus was derived from the ratio of the true stress and true strain values within the linear elastic range [28]. The standard errors were calculated from three measured samples for each type of the wires.

### 2.6. Measurements of electrical properties and current carrying capability

The room temperature electrical conductivity ( $\sigma_{RT}$ ) was calculated using the expression:  $\sigma_{RT} = 4 \times L / (\pi \times R \times d \times d)$ , where  $L = 10 \text{ mm}$  is the measured gauge length,  $R$  is the room temperature resistance measured using a Keithley 2400 SourceMeter under 4-wire configuration, and  $d$  is the mean diameter measured by SEM mentioned above. The standard errors were calculated from three measured samples for each type of the wires.

The current carrying capacity (ampacity) was determined by measuring the current density versus sweeping electric field ( $J$ - $E$ ). The stepwise  $J$ ,  $J$  response to stepwise  $E$  and  $J$  response to pulsed  $E$  were measured to evaluate the electrical fatigue properties. All the measurements above were performed under vacuum ( $10^{-4} \text{ Pa}$ ) by a Keithley 4200A-SCS equipped with a power transmission unit. Temperature rise induced by Joule-heating was measured by a non-contact infrared radiation thermometer (AST-AL47-4025, Beijing DHL Tech Co., Ltd.) with a precision of  $\pm 0.1\%$ . All the tested gauge length was set to  $20 \text{ mm}$ . Three samples were measured for each type of the wires. In addition, continuous current rating measurements were performed using the same setup but under  $150 \text{ sccm Ar}$  flow.

### 2.7. Measurements of thermal conductivity

Based on a well-established self-heating method [11,17,29], the thermal conductivity ( $\kappa$ ) was calculated using the expression:  $\kappa = QL/4A_c(T_m - T_a)$ , where  $Q$  is the applied electric power for self-heating of the wire sample,  $L = 20 \text{ mm}$  is the measured gauge length,  $A_c$  is the cross-sectional area, and  $T_m$  and  $T_a$  are the temperature at the middle point and the end of the wire, respectively. The measurement setup was similar to that used for the ampacity measurements under vacuum ( $10^{-4} \text{ Pa}$ ) but an infrared camera (Fluke TiS75) was used to measure the temperature profile along the wire axis. The standard errors were calculated from three measured samples for each type of the wires.

## 3. Results and discussion

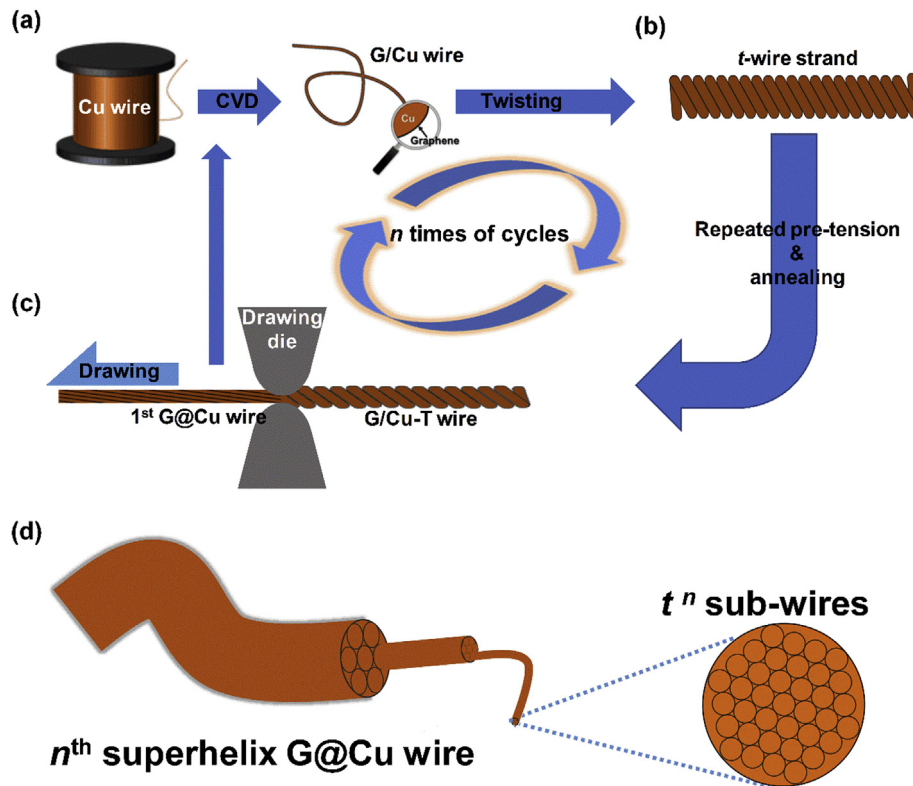
### 3.1. Fabrication and structure characterization

Fig. 1a–c illustrate the schematic cyclic growth-twisting-drawing fabrication procedure. Graphene coated Cu wires (G/Cu wires, Fig. 1a) were fabricated by the CVD process (see details in the Experimental section). A number ( $t$ ) of the G/Cu wires were twisted into helical strands ( $t$ -wire strands, Fig. 1b). The  $t$ -wire strands were subjected to repeated thermal-stretching treatment (see details in the Experimental section), which produced elongated and more tightly-packed helical strands (G/Cu-T wires, Fig. 1b). The G/Cu-T wires were subjected to multi-die drawing treatments (Fig. 1c). The helically arranged  $t$  wires were deformed to be closely packed with the graphene embedded within their interfaces, which involved synergistic effects to these wires including reduced diameter and elongation, accommodated radial plastic deformation to fill the voids, and adjusted helix angle. This produced graphene-inserted nanocomposite wires (1st superhelix G@Cu wires, Fig. 1c) composed of helically arranged  $t$  sub-wires with interfacial

graphene and possessing a uniform round outer shape with the same diameter as the die hole. Again, the CVD process was carried out with the 1st superhelix G@Cu wires, and the obtained samples were used for the next fabrication cycle. Replicating the above growth-twisting-drawing process  $n$  times generated superhelix graphene/Cu nanocomposite wires ( $n$ th superhelix G@Cu wires, Fig. 1d) composed of graphene-intercalated sub-wires (or fibers) in a total number that exponentially scales with  $n$ , as  $t^n$ . These sub-wires were progressively densified and their average diameter ( $d_a$ ) was remarkably reduced with increasing  $n$ , as  $d_a = D/t^{n/2}$ , where  $D$  is the diameter of the  $n$ th superhelix G@Cu wires. Meanwhile, graphene was replenished cyclically resulting in an increasing volume fraction ( $V_G$ ). The interfacial graphene layers were promoted to be closely spaced with reducing  $d_a$ , but distinctly separated. The sub-wires with their interfacial graphene were arranged with a micro texture of high order helix-upon-a-helix, known as superhelix [30], analogous to a hemp rope (Fig. 1d). Such structure characteristics favor uniform distribution and alignment of the graphene layers within the Cu matrix.

SEM images of the samples in each step of the first cycle are shown in Fig. 2a–c respectively. The CVD process produced graphene layers that uniformly covered the whole surface of the Cu wires, as indicated by the translucent surface of the G/Cu wires. Considering the imperfectness and the influence of the background (Cu or PMMA), Raman spectroscopy (sample 1, Fig. 2h) shows that the surface graphene are mainly multilayered and has a layer number of 2–3 and quite high quality, with the ratio  $I_{2D}/I_G = 0.85$  and low D peak at  $1350 \text{ cm}^{-1}$  [31,32,35]. The thermally stretched 6-wire strands (G/Cu-T wires, Fig. 2b) had a helix angle of  $37^\circ$  and overall diameter of  $\sim 600 \mu\text{m}$ , accompanying a  $\sim 20\%$  total elongation compared with the as twisted ones. The surface graphene layers appeared to be almost intact upon the repeated thermal-stretching process because the translucent surface exhibited little change after this treatment. Instead of the helix morphology, the obtained 1st superhelix G@Cu wires (Fig. 2c) had a continuous smooth surface and redefined diameter of  $\sim 200 \mu\text{m}$ , accompanying an overall 443–484% elongation compared with the G/Cu-T wires before the multi-die drawing treatment. However, pores and voids can be observed in the cross-section of the 1st superhelix G@Cu wire (bottom of Fig. 2c), which originated from the un-densified helical structure of the previous G/Cu-T wire (bottom of Fig. 2b). The subsequent CVD process produced surface graphene on the 1st superhelix G@Cu wires with identical quality and layers compared with that grown on the surface of the commercial Cu wires. Through 6 cycles of the growth-twisting-drawing procedure, the 6th superhelix G@Cu wires (top of Fig. 2d) possessed the same outer shape and dimension, and similar surface morphology as that of the 1st superhelix G@Cu wire (top of Fig. 2c), but a highly-densified cross-section without pores and voids (bottom of Fig. 2d).

The graphene layers were proved to be mostly continuous and uniformly distributed within the Cu matrix. Fig. 2e shows the 6th superhelix G@Cu wire after surface polishing and partial chemical etching. The magnified SEM image (Fig. 2f) demonstrates the rough surface resulting from the anisotropic corrosion. As shown in Fig. 2g, the typical EDS analysis within the measured area indicates that C element was uniformly distributed, which should only be the result of the existence of graphene inside the nanocomposite wire. The interior graphene has a similar layer number and quality as the surface graphene, which is proved by the almost unchanged characteristics comparing the Raman spectra of the PMMA/residuum and the blank PMMA samples (Fig. 2h) [31,32]. Additional EDS and Raman measurements were carried out repeatedly with different but adjacent locations spreading the sample wire. All the results showed identical characteristics and continuity/uniformity of the interior graphene within the measured areas. Importantly, it was



**Fig. 1.** Schematics of the fabrication process and structure of the superhelix graphene/Cu nanocomposite wires (superhelix G@Cu wires). (a), (b) and (c) successively demonstrate the cycled growth-twisting-drawing procedure.  $t$  is the number of the twisted wires. The obtained strand is repeatedly pre-tensioned and annealed before die drawing treatment.  $n$  is the total number of the cycles applied. (d) Schematic structure of the superhelix G@Cu wires fabricated by  $n$  cycles of the growth-twisting-drawing procedure, and the  $n$ th G@Cu wires should be seen as a bundle of massive, strongly bonded and super-helically arranged sub-wires in a total number of  $t^n$ .

found that there was no detectable missing/cracked area without graphene. These results show that the interior graphene is mostly continuous with a coverage ratio of  $\sim 100\%$ . Inevitably, there may be small missing/cracked areas without graphene that cannot be detected experimentally. However, these missing/cracked areas should be negligible compared with that covered with graphene, which should have negligible influence on the global continuity of the graphene. Although the repeated thermal-stretching and multi-die drawing treatments may lead to tensile fracture of graphene due to mismatched ductility of copper and graphene [32], the further cyclic CVD growth would repair not only the surface graphene but also the interior ones [33]. That is, most of the mechanically damaged graphene has been replenished and repaired cyclically to be almost continuous again. In addition, it was unlikely that chemical reactions occurred between the interior graphene and Cu matrix during the cyclic fabrication process [34,35]. Meanwhile, it was impossible for massive atomic diffusion and infiltration to occur across the interior graphene/Cu interfaces due to the poor wettability of C and Cu [22,36] and the fact that no thorough melting occurred during the whole procedure [35,37]. Moreover, the interior graphene restricted the recrystallization of the Cu matrix across the interface during high temperature annealing [22,23,27,38]. As a result, the final product  $n$ th superhelix G@Cu nanocomposite wires maintained the superhelix micro texture. And the interior graphene layers were highly uniformly distributed within the sub-wire interfaces and possessed good continuity spreading over the Cu matrix and maintained their coverage on the Cu crystal domains as they were initially grown. It is believed that such good continuity, together with the uniform

distribution/alignment and high quality, all are crucial to generate effective reinforcement to the mechanical and electrical properties discussed below. In contrast, the traditional die drawing process that simply densifies a composite wire [21] is unable to effectively modulate and refine the microscopic distribution of the nano inclusions. The planar stacking method is capable of generating nanocomposites with high aspect ratio, highly controllable alignment and interface spacing of the nano inclusions, but the method lacks the ability to produce long wires and fibers [26]. Most importantly, the repeated growth-twisting-drawing processes effectively avoided the agglomeration of the nano inclusions that considerably reduce reinforcement, compared with that by simple mixing or mechanical milling [35,39,40]. After all, the cycled growth-twisting-drawing process is a unique and outstanding method to produce one dimensional nanocomposite wires with full-scale control ability from macroscopic dimension down to microscopic structure.

Density measurements verified the high compactness of the superhelix nanocomposite wires. Fig. 2i shows the mass density of the  $n$ th superhelix G@Cu wires with increasing cycle number ( $n$ ), as well as comparing to that of the  $n$ th superhelix Cu wire controls. Statistically, both the density of the  $n$ th superhelix G@Cu wires and the  $n$ th superhelix Cu wire controls slightly decreased initially, mainly because of the un-fully densified structure (bottom of Fig. 2c) in the first few cycles. However, with increasing  $n$ , the density increased until quite close to that of the commercial Cu wire. The 6th superhelix G@Cu wires possessed a density of  $8.76 \text{ g cm}^{-3}$ , a negligible 0.2% lower than that of the commercial Cu wire, indicating the high compactness of the super-helically

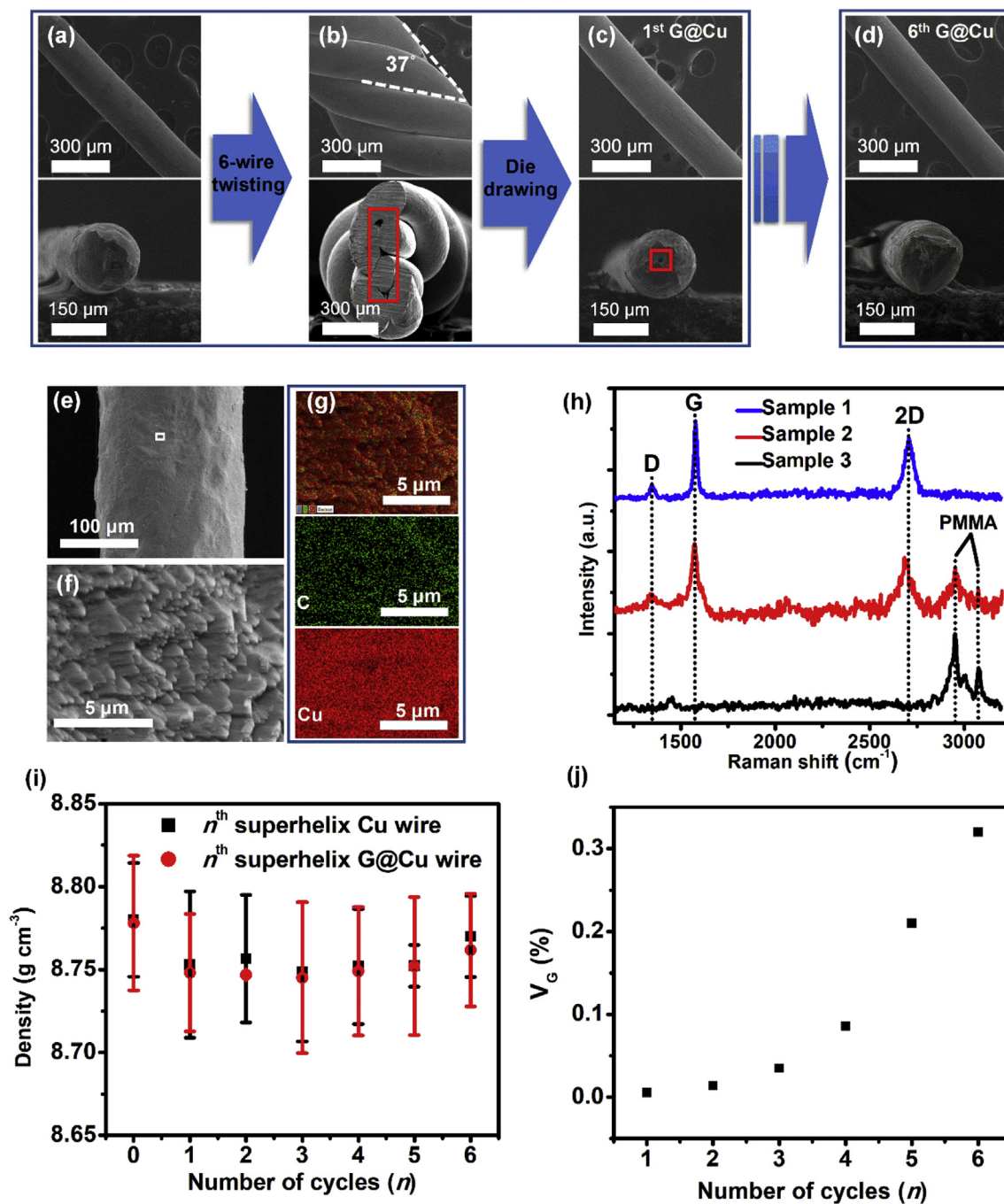


**Fig. 2.** Morphology and structure of the superhelix graphene/Cu nanocomposite wires. SEM images of (a) G/Cu wire, (b) G/Cu-T wire fabricated by repeated pre-tension and annealing of a 6-wire strand of the G/Cu wire in (a), (c) 1st superhelix G@Cu wire obtained by die drawing treatment of the G/Cu-T wire in (b), (d) 6th superhelix G@Cu wire fabricated by applying 6 cycles of the growth-twisting-drawing procedure. The upper and lower images respectively demonstrate the axial surface and cross-sectional morphology of the samples. The red rectangles in (b) and (c) indicate the pores and voids within the wires. (e) The SEM image of the surface morphology of the 6th superhelix G@Cu wire after surface etching and cleaning, and (f) the magnified SEM image of the denoted area (white rectangle) in (e). (g) The EDS results of the same zone of (f), showing the uniform and abundant distribution of C elements (introduced by graphene inside the composite wire) within the Cu matrix. (h) Raman spectra of graphene on the surface of the G/Cu wire (blue curve, sample 1), and PMMA adhered with interior graphene of the 6th superhelix G@Cu wire by etching of Cu thoroughly (red curve, sample 2), comparing to the referenced PMMA sample (black curve, sample 3). (i) Density of the G/Cu and  $n^{\text{th}}$  superhelix G@Cu wires with increased number ( $n$ ) of cycles (red points), and referenced Cu and  $n^{\text{th}}$  superhelix Cu wires by the same treatments but without graphene (black points). (j) Graphene volume fraction ( $V_G$ ) of the  $n^{\text{th}}$  superhelix G@Cu wires with increasing number ( $n$ ) of cycles.

arranged sub-wires. The cyclic multi-die drawing treatment and high temperature ( $1000^\circ\text{C}$ ) during the CVD procedure elevated interfacial contact and resulted in the high compactness of these sub-wires.

The graphene volumetric fraction ( $V_G$ ) was estimated based on the idealized superhelix structure that excludes void space and

pores, in which the sub-wires are almost completely covered with interfacial graphene with a layer number of 2–3. The  $n^{\text{th}}$  superhelix G@Cu wire possesses  $6^n$  sub-wires, for example  $6^6 = 46656$ . The mean diameter of the sub-wires ( $d_a$ ) was estimated by approximately average the total cross-sectional area of the  $n^{\text{th}}$  superhelix G@Cu wire to  $6^n$  individual sub-wires. The mean

diameter of the sub-wires of the 6th superhelix G@Cu wire is estimated to be  $\sim 0.92 \mu\text{m}$ . The volume fraction ( $V_G$ , Fig. 2j) was estimated to be up to  $\sim 0.32\%$  for a cycle number of 6. The true graphene volume fraction should be close to but no more than the idealized values ( $\sim 0.32\%$ ), considering the void space and pores and tiny missing/cracked areas without graphene. The graphene volumetric fraction ( $V_G$ ) of the superhelix nanocomposite wires increases with increasing cycle number ( $n$ ) (Fig. 2j). This is because the mean diameter of the sub-wires ( $d_a$ ) is considerably reduced with increasing cycle numbers ( $n$ ), while the interfacial graphene maintained a coverage ratio of  $\sim 100\%$  (almost continuous) after finishing the fabrication processes. Further increasing  $V_G$  with more refined superhelix micro structure down to nanometer or even the primitive cell scale by increasing the cycle number are expected to be possible in principle, as has been collaterally evidenced by previous reports on nanolayered systems [25,41]. In brief, the superhelix nanocomposite wires substantially take advantage of controllable and uniform distribution and alignment with increasing volumetric fraction of the nano inclusions while maintaining the superhelix structure. Such improved structure quality with the excellent properties of the CVD graphene contribute to the superior properties of the nanocomposite wire.

### 3.2. Mechanical properties

Monotonic tensile tests were performed to evaluate the mechanical properties. The true stress-strain curves of the  $n$ th superhelix G@Cu wires were measured (Fig. 3a), as well as comparing to

that of the  $n$ th superhelix Cu wires (Fig. 3b). The Young's modulus ( $E$ ), maximum true stress ( $\sigma$ ) and maximum true strain ( $\epsilon$ ) were derived from the true stress-strain curves (Fig. 3c–e). Both the  $n$ th superhelix G@Cu wires and  $n$ th superhelix Cu wires demonstrated decreases in  $E$  (Fig. 3c) but increases in  $\sigma$  (Fig. 3d) with increasing  $V_G$ . The initial declines of both  $E$  and  $\sigma$  values mainly resulted from reduced density (Fig. 2i). Furthermore, the  $n$ th superhelix G@Cu wires exhibit larger reduction in stiffness and increase in strength than the  $n$ th superhelix Cu wire controls. The 6th superhelix G@Cu wires ( $V_G = \sim 0.32\%$ ) have considerably reduced  $E$ , with  $E/E_{\text{com, Cu}} = 100.3/196.2$  (GPa/GPa) and  $E/E_{6, \text{Cu}} = 100.3/152.3$  (GPa/GPa), corresponding to a decrease in stiffness by 49% and 34% respectively (Fig. 3c). On the other hand, there is a moderately improved  $\sigma = 270$  MPa, compared with  $\sigma_{\text{com, Cu}} = 245$  MPa and  $\sigma_{6, \text{Cu}} = 247$  MPa, or 10% and 9% increase in strength respectively (Fig. 3d). Moreover, the  $n$ th superhelix G@Cu wires and  $n$ th superhelix Cu wires demonstrated similar improvements in ductility, both exhibiting the highest increase  $\Delta\epsilon = \sim 9\%$ , or  $\sim 80\%$  increase from that of the commercial Cu wire (Fig. 3e). These results indicate both improvements in ductility and reductions in stiffness with the superhelix structure, and enhanced strengthening effects with the interfacial graphene layers.

Both the  $n$ th superhelix wires with and without graphene demonstrated improved mechanical strength with increasing cycle numbers. However, the  $n$ th superhelix G@Cu wires showed moderately larger improvement. These results indicated that the superhelix structure contributed to the strengthening effects, which was further enhanced by the interfacial graphene layers. The

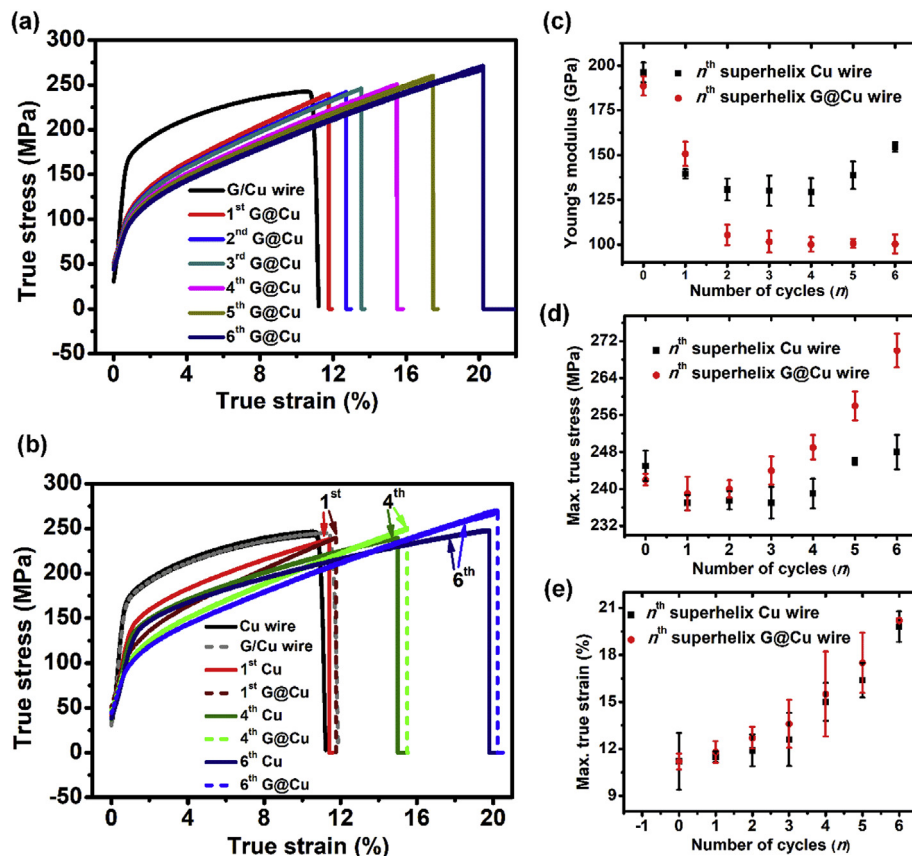


**Fig. 3.** Mechanical properties of the superhelix graphene/Cu nanocomposite wires. (a) True stress-strain curves of the G/Cu wire and  $n$ th superhelix G@Cu wires with increased number ( $n$ ) of cycles. (b) Comparison of the true stress-strain curves of the  $n$ th superhelix G@Cu wires and  $n$ th superhelix Cu wires, including the G/Cu and commercial Cu wires. (c) The Young's modulus, (d) maximum true stress, and (e) maximum true strain of the G/Cu ( $n = 0$ ) and  $n$ th superhelix G@Cu wires with increased number ( $n$ ) of cycles (red points), and referenced commercial Cu ( $n = 0$ ) and  $n$ th superhelix Cu wires by the same treatments but without graphene (black points).

strengthening effect essentially occurs because of the high intrinsic strength and nano-confinement effects of graphene [25,31,32,39]. On one hand, the strong C–C bond network of graphene layers act as a much larger barrier than grain boundary to constrain dislocation propagation across the graphene/Cu interface [39–42]. On the other hand, graphene layers hinder the growth and recrystallization of the Cu crystal grains during the high-temperature annealing as discussed above, and the matrix can be strengthened by decreasing the crystal grain size (grain-boundary strengthening) in terms of the Hall–Petch relation [22,28,39]. As a result, like other reported graphene and CNTs reinforced composites [31,33,38,39], it is believed that both the greatly reduced grain size and enhanced grain-boundary strengthening by graphene contribute to the high strength of the nanocomposite wires [41,43–47].

### 3.3. Electrical conductivity and current carrying capacity

The  $n$ th superhelix G@Cu wires show negligible decreases in room temperature electrical conductivity ( $\sigma_{RT}$ ) due to the vanishingly small  $V_G$  and high density (Fig. 4a) compared to the commercial Cu wire. The 6th superhelix G@Cu wires ( $V_G = \sim 0.32\%$ ) exhibit a value of  $5.01 \times 10^7 \text{ S m}^{-1}$ , less than a 12% reduction from that of the commercial Cu wire and comparable to that of pure Copper ( $5.80 \times 10^7 \text{ S m}^{-1}$ ) [48]. This value is 2–3 orders of magnitude higher than the CNTs/Cu composites by electrodeposition and sputtering [1,11,21,37,49], and even 10–20% higher than the

Graphene/Cu composites by powder metallurgy [22,39].

Central to this study, it is found that the superhelix graphene/Cu nanocomposite wires exhibit largely improved ampacity compared to that of the commercial Cu wire. The current density–electric field ( $J$ - $E$ ) curves of the  $n$ th superhelix G@Cu wires (Fig. 4b) were measured, as well as comparing to that of the  $n$ th superhelix Cu wires (Fig. 4c). Electric fields were applied to generate considerable current-induced temperature rise (Joule-heating) until the wires fused at a maximum current density ( $J_m$ ). Large improvements in ampacity were observed, that is,  $J_m$  increases remarkably with increasing  $V_G$  (Fig. 4b–c). The 6th superhelix G@Cu wires ( $V_G = \sim 0.32\%$ ) show about 200% increase in ampacity ( $\sim 5.8 \times 10^{10} \text{ A m}^{-2}$ , compared with  $\sim 2.2 \times 10^{10} \text{ A m}^{-2}$  of the commercial Cu wires). As shown in Fig. 4d, the ampacity vs conductivity plots demonstrate an inverse trend with conventional metals and nano carbons. That is, metals possess higher conductivities and nano carbons possess higher ampacities. Our superhelix nanocomposite wires stand out with both outstanding conductivity and ampacity. Notably, the ampacity of the 6th superhelix G@Cu wires is about 220–310% of that of conventional conductors, such as Cu, Al, Au and Ag ( $\sim 10^{10} \text{ A m}^{-2}$ ) [3,4,58,64,66]. That is also  $\sim 5$  times and  $\sim 2$  orders of magnitude higher than that of conventional graphene/Cu fibers [17] and SWNT/Cu fibers [21] respectively, except for that of the reported CNT-Cu ( $6 \times 10^{12} \text{ A m}^{-2}$ ) with a large volume fraction (45%) of CNTs [1]. In contrast to most of the reports [11,37,50–53] on high ampacity that make compromise to low conductivity, we succeeded in achieving high ampacity while maintaining an electrical

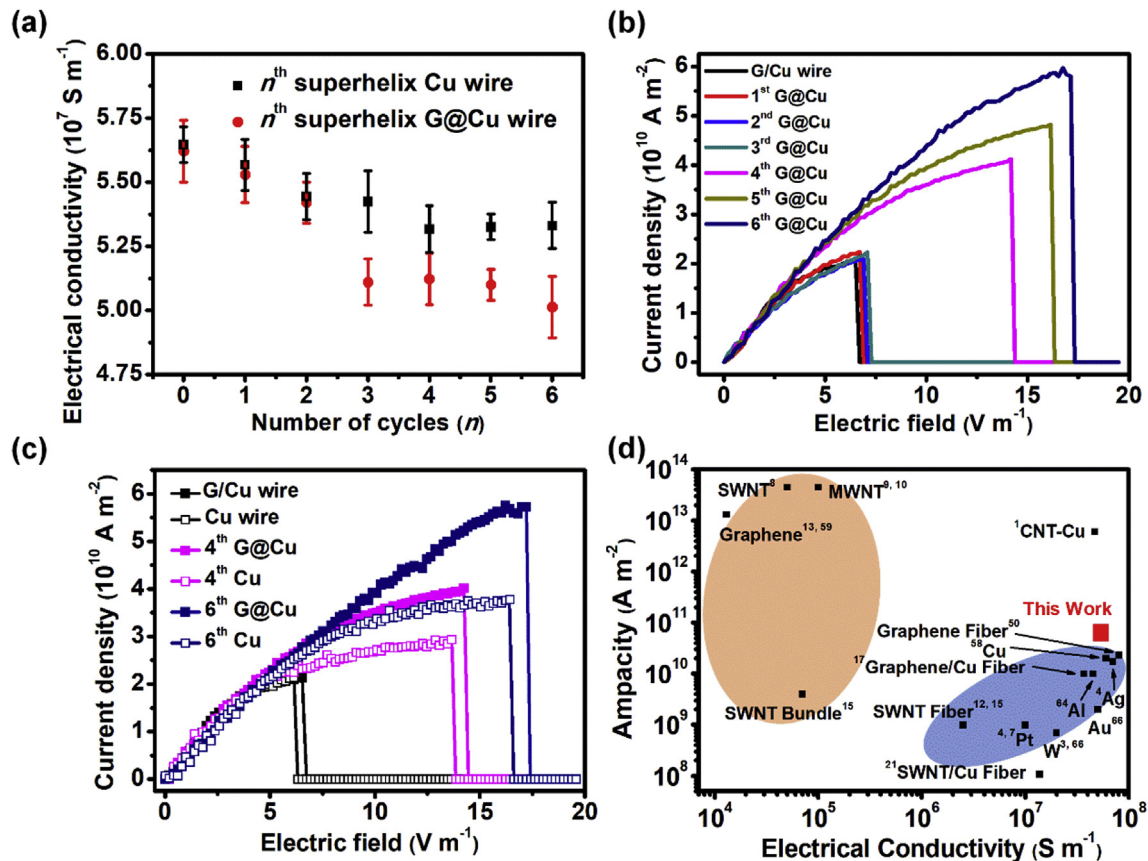


**Fig. 4.** Electrical properties and current density versus electric field ( $J$ - $E$ ) characteristics of the superhelix graphene/Cu nanocomposite wires. (a) Electrical conductivity of the G/Cu ( $n = 0$ ) and  $n$ th superhelix G@Cu wires with increased number ( $n$ ) of cycles (red points), and referenced commercial Cu ( $n = 0$ ) and  $n$ th superhelix Cu wires by the same treatments but without graphene (black points). (b)  $J$ - $E$  curves of the G/Cu and  $n$ th superhelix G@Cu wires with increased number ( $n$ ) of cycles. (c) Comparison of the  $J$ - $E$  curves of the  $n$ th superhelix G@Cu wires and  $n$ th superhelix Cu wires, including the G/Cu and commercial Cu wires. (d) Ampacity vs conductivity plots compared with conventional metals, nano carbons, and nano carbon based composite wires.

conductivity comparable to that of pure copper. There is still large promotion space to maximumly improve the ampacity of our superhelix nanocomposite wires as proposed theoretically [54] by further increasing the volume fraction of graphene.

### 3.4. Mechanism of high current carrying capacity

Such considerably improved ampacity can be mainly attributed to the suppressed electromigration and thermal diffusion of Cu atoms by the interfacial graphene layers. For pure Cu, electromigration occurs at the surfaces and grain boundaries that significantly reduce the conductivity [55–58], which considerably elevates the Joule-heating effect. Results shown in this study indicate the Cu migration pathways through surface and grain boundaries were greatly suppressed by the interfacial graphene layers. In addition, graphene itself has excellent ampacity, close to copper [59]. And the adhesion between graphene and Cu are excellent due to strong interaction [60], which considerably prevent thermal oxidation under Joule-heating [61]. The average temperature ( $T_{avg}$ ) along the wire axis was captured accompanying the  $J$ - $E$  measurements. There are large different current densities for these wires to reach a same temperature (Fig. 5a). For example, the commercial Cu wire reached a temperature of  $\sim 995.7^\circ\text{C}$  at a current density of  $\sim 1.9 \times 10^{10} \text{ A m}^{-2}$ ; in contrast, at the same level of temperature ( $\sim 974.9^\circ\text{C}$ ), the 6th superhelix G@Cu wire could have a much higher current density of  $\sim 4.9 \times 10^{10} \text{ A m}^{-2}$  (Fig. 5a). It was found that all these wires fused at almost identical temperatures around the melting point of copper ( $1084^\circ\text{C}$ ) [48], determined by the composite matrix. This indicates such low  $V_G$  ( $\sim 0.32\%$ ) have negligible influence on the overall thermal stability and melting point of the composite, which is distinguished from the cases that large inclusion contents restrict thermal diffusion in a

bulk scale. The improved ampacity then comes from suppressed electromigration near the graphene/Cu interfaces, which was considerably enhanced with increasing  $V_G$ . The mechanism was verified through investigation into the non-linear relationship  $\sigma$ - $T$  from RT to  $\sim 1273 \text{ K}$ . Fig. 5b shows the plots of electric conductivity (normalized to the RT one,  $\sigma(T)/\sigma_{RT}$ ) versus temperature (average temperature rise measured from RT,  $\Delta T_{avg}$ ), as well as the non-linear curve fitting of each tested sample. Non-linear curve fittings give the temperature coefficient of resistivity ( $\alpha$ ) for each sample (Fig. 5c). Notably, the  $n$ th superhelix G@Cu wires show considerably reduced  $\alpha$  value with increasing  $V_G$ . The mean  $\alpha$  value of the 6th superhelix G@Cu wire is 0.00234,  $\sim 5\%$  and  $58\%$  of that of the commercial Cu wire and pure copper ( $\sim 0.00399$ – $0.00433$ ) [59], which is also clearly shown by the outstanding fitting curve of the 6th superhelix G@Cu wire. The significantly lower  $\alpha$  value indicates smaller decreases in conductivity at high current density, which correspond to suppressed electromigration near the graphene/Cu interfaces. Theoretical studies have proposed that the activation energy for carbon-doped Cu diffusion increases by suppressing surface and grain boundary pathways [57,60,61]. It is believed that the graphene in the superhelix nanocomposite wires has a similar function in suppressing Cu electromigration [62–64].

### 3.5. Electric fatigue properties

Any current density or that conducted by an electric field less than  $J_m$  results in fatigue failure instead of immediate fusing. The fatigue experiments under stepped  $J$  (Fig. 6a) and  $E$  (Fig. 6b), and pulsed  $E$  (Fig. 6c–d) were measured under vacuum ( $10^{-4} \text{ Pa}$ ). At a constant  $J = 5.5 \times 10^{10} \text{ A m}^{-2}$ , the 6th superhelix G@Cu wire breaks down after  $\sim 350 \text{ s}$ , below which the sample conducts for at least  $600 \text{ s}$  with negligible degradation (Fig. 6a). For the case of 6th

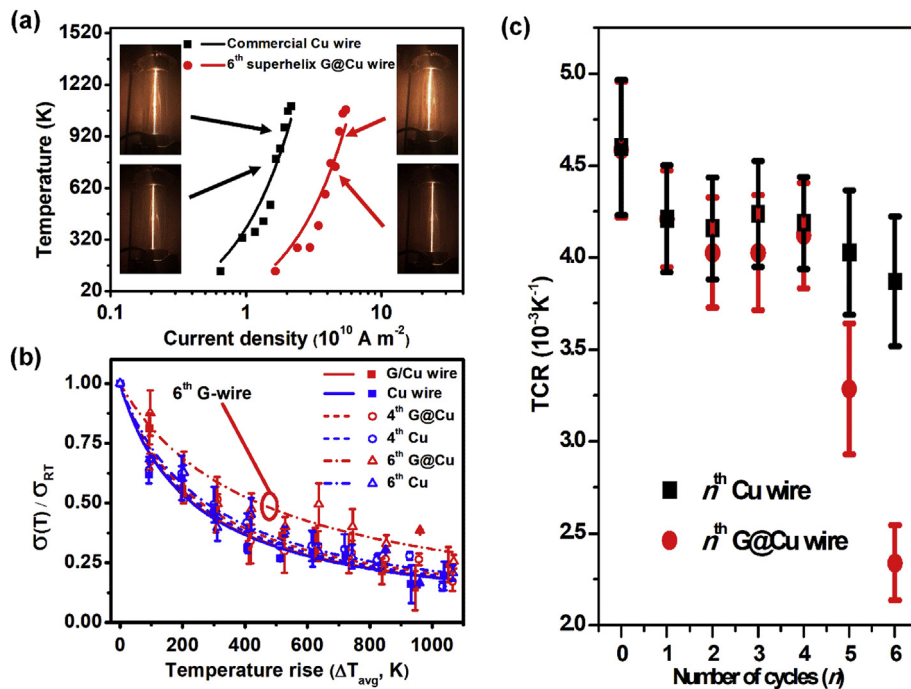


**Fig. 5.** Temperature coefficient of resistivity of the superhelix graphene/Cu nanocomposite wires. (a) Measured temperature versus current density of the 6th superhelix G@Cu wires and commercial Cu wires, and the corresponding linear fittings. The inset photographs demonstrate the 6th superhelix G@Cu wire and commercial Cu wires perform equivalent thermal radiation luminescence at the same temperature by Joule-heating, at which the 6th superhelix G@Cu wire is carrying larger current density than the commercial Cu wire. (b) Measured electric conductivity (normalized to the room temperature value) plotted as a function of the average temperature rise by Joule-heating of the samples, and fitting curves. (c) Calculated temperature coefficient of resistance (TCR) of the samples, based on the results in (a).

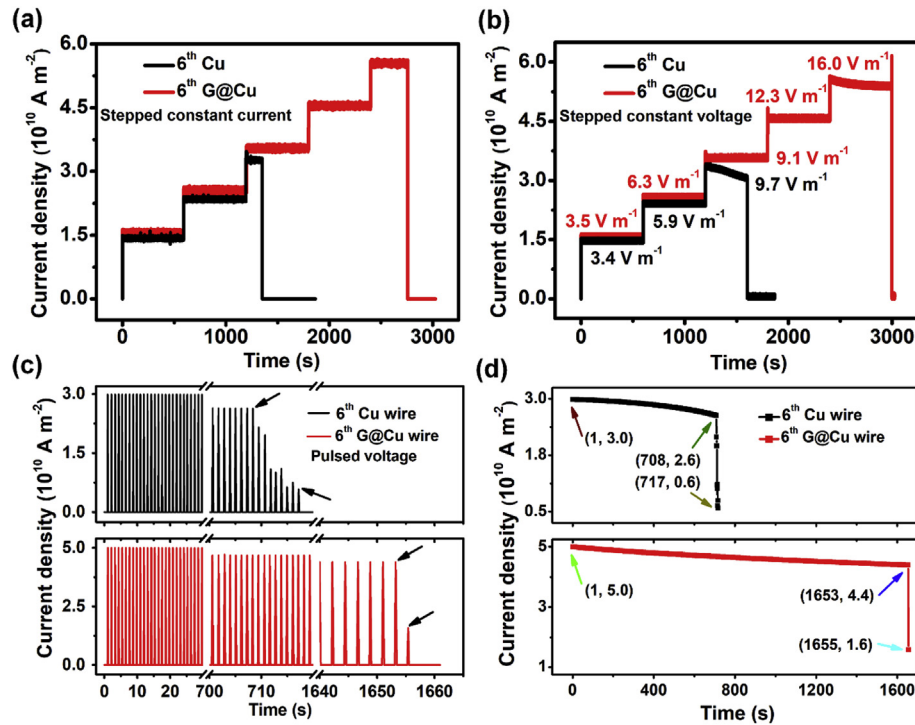


**Fig. 6.** Fatigue properties and current carrying capability of the superhelix graphene/Cu nanocomposite wires. Current density versus time measurements of the 6th superhelix G@Cu wire and 6th superhelix Cu wire with step-wised constant current source (a) and constant voltage source (b), and 600 s duration for each step. (c) Current density response to pulsed voltage source of the 6th superhelix G@Cu wire (upper, black) and 6th superhelix Cu wire (lower, red), using a 0.9 Hz frequency and 9% duty ratio. (d) The responding peak current density in (c) are plotted to demonstrate the pulse fatigue properties. The corresponding colored arrows point to the same peaks in (c).

superhelix Cu wire, the break down current density is only  $3.2 \times 10^{10} \text{ A m}^{-2}$  and 150 s duration (Fig. 6a). Under break down electric field (Fig. 6b), the 6th superhelix G@Cu wire also exhibits longer duration up to 580 s, compared with 400 s for the 6th superhelix Cu wire, though both output powers were moderately reduced by thermally induced increase in resistance (Fig. 6b). These superior fatigue resistivity of the 6th superhelix G@Cu wires indicate the electromigration is efficiently suppressed by the graphene/Cu interfaces that substantially improve the ampacity. Moreover, the 6th superhelix G@Cu wire persists in function under a pulsed  $E$  of  $11 \text{ V m}^{-1}$  for  $\sim 1500$  cycles, while only  $\sim 640$  cycles under a lower  $E$  of  $7.5 \text{ V m}^{-1}$  for the 6th superhelix Cu wire (Fig. 6c). Both wires demonstrate  $\sim 10\%$  decreased peak current density (Fig. 6d) before breaking down, which resulted from the accumulated degradation to the samples due to both the electromigration/diffusion and high-frequency thermally induced stress and deformation [15,16,65]. Taking the advantages of combined superior mechanical properties and ampacity, the graphene/Cu nanocomposite wires promise wide applications in the areas of heavy-duty and high-frequency/power.

### 3.6. Continuous current rating

For practical applications, it is the balance between the heating current and the thermal dissipation into the surroundings that determines the continuous current rating of the current-carrying wire [12]. The  $n$ th superhelix G@Cu wires possess comparable thermal conductivity to the commercial Cu-wires, though their values slightly decreased with increasing  $V_G$  (Fig. 7a). The average temperature rises of the electrically heated wire ( $\Delta T_{\text{avg}}$ ) versus the square of current density are shown in Fig. 7b, which gives linear relationships for all the tested wires with different slopes. Based on natural convection theory [12], the thermal conductance ( $g$ )

between the electrically heated wires and the Ar atmosphere can be derived, which give nearly identical thermal conductance ( $g$ ),  $39\text{--}42 \text{ W m}^{-2} \text{ K}^{-1}$  of the  $n$ th superhelix G@Cu wires and  $n$ th superhelix Cu wires independent on  $V_G$  (Fig. 7c). This indicates the fact that the thermal conductance solely depends on the wire diameter and gas conditions, considering the negligible difference of the thermal conductivity. With the above determined values for  $g$ , together with the temperature-dependent electric conductivity, the continuous current rating can be calculated for a given operating temperature,  $T_0$  [12]. At  $T_0 = 360 \text{ K}$ , the calculated continuous current rating value of the 6th superhelix G@Cu wire is  $1.9 \times 10^{10} \text{ A m}^{-2}$ , about 1.7 times of that of the commercial Cu wire ( $1.1 \times 10^{10} \text{ A m}^{-2}$ ), which agrees well with the measured values (Fig. 7d).

## 4. Conclusions

Using a novel cyclic growth-twisting-drawing strategy, we succeeded in fabricating nanocomposite wires with largely improved current carrying capacity, uncompromised electrical conductivity and enhanced mechanical performance. Such improved comprehensive properties can be attributed to the superhelix micro structure and nano-confinement effect of the interfacial graphene. These results highlight the importance of the superhelix nanocomposite material structure and the atomic thin graphene interfaces. In future work, higher strength and ampacity may be achieved if the wire is drawn through a much smaller hole during a further modified processing. For example, the annealing treatment can be introduced between the different drawing treatments. Overall, the superhelix graphene/Cu nanocomposite wires fabricated by the proposed method in this work possess excellent comprehensive performance, bringing about prosperous

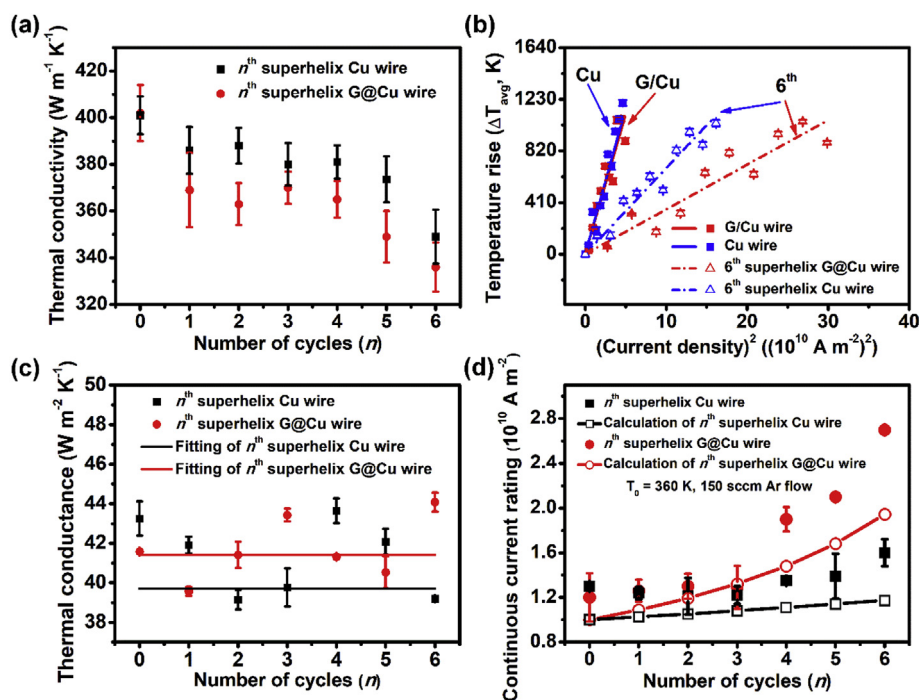


**Fig. 7.** Determination of the continuous current rating of the superhelix graphene/Cu nanocomposite wires. (a) Thermal conductivity of the G/Cu and  $n^{\text{th}}$  superhelix G@Cu wires with increasing cycle number ( $n$ ) (red points), and referenced commercial Cu and  $n^{\text{th}}$  superhelix Cu wires by the same treatments but without graphene (black points). (b) Measured average temperature rise of the samples plotted as a function of the square of the applied current density, and the simulated linear relationships. (c) Calculated thermal conductance ( $g$ ) between the current-carrying wires and surrounding Ar flow, the lines are least square fittings of the calculated values. (d) The measured continuous current rating of the superhelix graphene/Cu nanocomposite wires and referenced wires without graphene (solid points), and the calculated values (hollow points).

applications, such as alternative graphene-based materials to replace copper and/or other metal materials that widely used for conducting wires/cables in many fields.

## Acknowledgements

The authors gratefully acknowledge the financial support from Ministry of Science and Technology of China (MoST, 2016YFA0200200), the National Natural Science Foundation of China (NSFC, 21421001, 51633002, and 51472124), 111 Project (B12015), and Tianjin city (16ZXCLGX00100).

## References

- [1] C. Subramaniam, T. Yamada, K. Kobashi, A. Sekiguchi, D.N. Futaba, M. Yumura, et al., One hundred fold increase in current carrying capacity in a carbon nanotube-copper composite, *Nat. Commun.* 4 (2013) 2202.
- [2] A. Sedaghat, F. de Leon, Thermal analysis of power cables in free air: evaluation and improvement of the IEC standard ampacity calculations, *IEEE Trans. Power Deliv.* 29 (5) (2014) 2306–2314.
- [3] H.B. Huntington, A.R. Grone, Current-induced marker motion in gold wires, *J. Phys. Chem. Solid.* 20 (1) (1961) 76–87.
- [4] P.S. Ho, T. Kwok, Electromigration in metals, *Rep. Prog. Phys.* 52 (3) (1989) 301.
- [5] R. Hoerauf, Ampacity application considerations for underground cables, *IEEE Trans. Ind. Appl.* 52 (6) (2016) 4638–4645.
- [6] H. Brakelmann, G. Anders, Ampacity reduction factors for cables crossing thermally unfavorable regions, *IEEE Trans. Power Deliv.* 16 (4) (2001) 444–448.
- [7] J.R. Lloyd, J.J. Clement, Electromigration in copper conductors, *Thin Solid Films* 262 (1–2) (1995) 135–141.
- [8] Z. Yao, C.L. Kane, C. Dekker, High-field electrical transport in single-wall carbon nanotubes, *Phys. Rev. Lett.* 84 (13) (2012) 2941–2944.
- [9] B.Q. Wei, R. Vajtai, P.M. Ajayan, Reliability and current carrying capacity of carbon nanotubes, *Appl. Phys. Lett.* 79 (8) (2001) 1172–1174.
- [10] P.G. Collins, M. Hersam, M. Arnold, R. Martel, P. Avouris, Current saturation and electrical breakdown in multiwalled carbon nanotubes, *Phys. Rev. Lett.* 86 (14) (2001) 3128–3131.
- [11] G. Xin, T. Yao, H. Sun, S.M. Scott, D. Shao, G. Wang, et al., Highly thermally conductive and mechanically strong graphene fibers, *Science* 349 (6252) (2015) 1083–1087.
- [12] X. Wang, N. Behabtu, C.C. Young, D.E. Tsentelovich, M. Pasquali, J. Kono, High-ampacity power cables of tightly-packed and aligned carbon nanotubes, *Adv. Funct. Mater.* 24 (21) (2014) 3241–3249.
- [13] V.E. Dorgan, A. Behnam, H.J. Conley, K.I. Bolotin, E. Pop, High-field electrical and thermal transport in suspended graphene, *Nano Lett.* 13 (10) (2013) 4581–4586.
- [14] L. Pauling, *The Nature of the Chemical Bond*, third ed., Cornell University Press, Ithaca, 1960.
- [15] P. Jarosz, C. Schauerman, J. Alvarenga, B. Moses, T. Mastrangelo, R. Raffaele, et al., Carbon nanotube wires and cables: near-term applications and future perspectives, *Nanoscale* 3 (11) (2011) 4542–4553.
- [16] C.D. Cress, M.J. Ganter, C.M. Schauerman, K. Soule, J.E. Rossi, C.C. Lawlor, et al., Carbon nanotube wires with continuous current rating exceeding 20 Amperes, *J. Appl. Phys.* 122 (2) (2017), 025101.
- [17] S.J. Kim, D.H. Shin, Y.S. Choi, H. Rho, M. Park, B.J. Moon, et al., Ultrastrong graphene-copper core-shell wires for high-performance electrical cables, *ACS Nano* 12 (3) (2018) 2803–2808.
- [18] K. Lü, G. Zhao, X. Wang, A brief review of graphene-based material synthesis and its application in environmental pollution management, *Chin. Sci. Bull.* 57 (11) (2012) 1223–1234.
- [19] L.M. Peng, Z.Y. Zhang, S. Wang, X.L. Liang, Carbon based nanoelectronics: materials and devices, *Sci. Sin.* 44 (10) (2014) 1071–1086.
- [20] Y. Ma, Y. Chen, Three-dimensional graphene networks: synthesis, properties and applications, *Nat. Sci. Rev.* 2 (1) (2015) 40–53.
- [21] B. Han, E. Guo, X. Xue, Z. Zhao, L. Luo, H. Qu, et al., Fabrication and densification of high performance carbon nanotube/copper composite fibers, *Carbon* 123 (2017) 593–604.
- [22] Y. Chen, X. Zhang, E. Liu, C. He, C. Shi, J. Li, et al., Fabrication of in-situ grown graphene reinforced Cu matrix composites, *Sci. Rep.* 6 (2016) 19363.
- [23] D.B. Xiong, M. Cao, Q. Guo, Z. Tan, G. Fan, Z. Li, et al., Graphene-and-copper artificial nacre fabricated by a preform impregnation process: bioinspired strategy for strengthening-toughening of metal matrix composite, *ACS Nano* 9 (7) (2015) 6934–6943.
- [24] J. Zou, D. Liu, J. Zhao, L. Hou, T. Liu, X. Zhang, et al., Ni nanobuffer layer provides light-weight CNT/Cu fibers with superior robustness, conductivity, and ampacity, *ACS Appl. Mater. Interfaces* 10 (9) (2018) 8197–8204.
- [25] Y. Kim, J. Lee, M.S. Yeom, J.W. Shin, H. Kim, Y. Cui, et al., Strengthening effect of single-atomic-layer graphene in metal-graphene nanolayered composites, *Nat. Commun.* 4 (2013) 2114.
- [26] P. Liu, Z. Jin, G. Katsukis, L.W. Drahushuk, S. Shimizu, C.J. Shih, et al., Layered and scrolled nanocomposites with aligned semi-infinite graphene inclusions

- at the platelet limit, *Science* 353 (6297) (2016) 364–367.
- [27] X. Li, W. Cai, J. An, S. Kim, J. Nah, D. Yang, et al., Large-area synthesis of high-quality and uniform graphene films on copper foils, *Science* 324 (5932) (2009) 1312–1314.
- [28] J.R. Greer, W.C. Oliver, W.D. Nix, Size dependence of mechanical properties of gold at the micron scale in the absence of strain gradients, *Appl. Phys. A* 80 (8) (2005) 1625–1629.
- [29] L. Lu, M.L. Sui, K. Lu, Superplastic extensibility of nanocrystalline copper at room temperature, *Science* 287 (5457) (2000) 1463–1466.
- [30] A. Kikuchi, K. Asai, Reverse gyrase—a topoisomerase which introduces positive superhelical turns into DNA, *Nature* 309 (5970) (1984) 677–681.
- [31] U. Moger, R. Dhanya, R. Pujar, C. Narayana, G.U. Kulkarni, Highly decoupled graphene multilayers: turbostraticity at its best, *J. Phys. Chem. Lett.* 6 (21) (2015) 4437–4443.
- [32] X. Xu, C. Lin, R. Fu, S. Wang, R. Pan, G. Chen, et al., A simple method to tune graphene growth between monolayer and bilayer, *AIP Adv.* 6 (2) (2016), 025026.
- [33] J. Hwang, T. Yoon, S.H. Jin, J. Lee, T.S. Kim, S.H. Hong, et al., Enhanced mechanical properties of graphene/copper nanocomposites using a molecular-level mixing process, *Adv. Mater.* 25 (46) (2013) 6724–6729.
- [34] A. Guillet, E.Y. Nzoma, P. Pareige, A new processing technique for copper–graphite multifilamentary nanocomposite wire: microstructures and electrical properties, *J. Mater. Process. Technol.* 182 (1–3) (2007) 50–57.
- [35] W.J. Kim, T.J. Lee, S.H. Han, Multi-layer graphene/copper composites: preparation using high-ratio differential speed rolling, microstructure and mechanical properties, *Carbon* 69 (2014) 55–65.
- [36] C.L. Pavithra, B.V. Sarada, K.V. Rajulapati, T.N. Rao, G. Sundararajan, A new electrochemical approach for the synthesis of copper–graphene nanocomposite foils with high hardness, *Sci. Rep.* 4 (2014) 4049.
- [37] Y. Zhu, S. Murali, W. Cai, X. Li, W.S. Ji, J.R. Potts, et al., Graphene and graphene Oxide: synthesis, properties, and applications, *Adv. Mater.* 22 (35) (2010) 3906–3924.
- [38] H. Kwon, M. Estili, K. Takagi, T. Miyazaki, A. Kawasaki, Combination of hot extrusion and spark plasma sintering for producing carbon nanotube reinforced aluminum matrix composites, *Carbon* 47 (3) (2009) 570–577.
- [39] K. Chu, C. Jia, Enhanced strength in bulk graphene–copper composites, *Phys. Status Sol. a* 211 (1) (2014) 184–190.
- [40] Y. Tang, X. Yang, R. Wang, M. Li, Enhancement of the mechanical properties of graphene–copper composites with graphene–nickel hybrids, *Mater. Sci. Eng. A* 599 (2014) 247–254.
- [41] J.S. Carpenter, A. Misra, P.M. Anderson, Achieving maximum hardness in semi-coherent multilayer thin films with unequal layer thickness, *Acta Mater.* 60 (6–7) (2012) 2625–2636.
- [42] N.J. Petch, The cleavage strength of polycrystals, *J. Iron Steel Inst.* 174 (1) (1953) 25–28.
- [43] A. Misra, J.P. Hirth, R.G. Hoagland, Length-scale-dependent deformation mechanisms in incoherent metallic multilayered composites, *Acta Mater.* 53 (18) (2005) 4817–4824.
- [44] N.A. Mara, D. Bhattacharyya, J.P. Hirth, P. Dickerson, A. Misra, Mechanism for shear banding in nanolayered composites, *Appl. Phys. Lett.* 97 (2) (2010) 2935.
- [45] A. Misra, J.P. Hirth, H. Kung, Single-dislocation-based strengthening mechanisms in nanoscale metallic multilayers, *Philos. Mag. A* 82 (16) (2002) 2935–2951.
- [46] R.G. Hoagland, R.J. Kurtz, C.H.H. Jr, Slip resistance of interfaces and the strength of metallic multilayer composites, *Scripta Mater.* 50 (6) (2004) 775–779.
- [47] S.M. Han, M.A. Phillips, W.D. Nix, Study of strain softening behavior of Al–AlSiC multilayers using microcompression testing, *Acta Mater.* 57 (15) (2009) 4473–4490.
- [48] R.C. Weast, *Handbook of Chemistry and Physics*, 64th ed., CRC Press, Florida, 1983.
- [49] W. Steinhögl, G. Schindler, G. Steinlesberger, M. Engelhardt, Size-dependent resistivity of metallic wires in the mesoscopic range, *Phys. Rev. B* 66 (7) (2002) 429–436.
- [50] Z. Xu, Y. Liu, X. Zhao, L. Peng, H. Sun, Y. Xu, et al., Ultrastiff and strong graphene fibers via full-scale synergetic defect engineering, *Adv. Mater.* 28 (30) (2016) 6449–6456.
- [51] R.S. Lee, H.J. Kim, J.E. Fischer, A. Thess, R.E. Smalley, Conductivity enhancement in single-walled carbon nanotube bundles doped with K and Br, *Nature* 388 (6639) (1997) 255–257.
- [52] H. Dai, E.W. Wong, C.M. Lieber, Probing electrical transport in nanomaterials: conductivity of individual carbon nanotubes, *Science* 272 (5261) (1996) 523–526.
- [53] N. Behabtu, C.C. Young, D.E. Tsentelovich, O. Kleinerman, X. Wang, A.W. Ma, et al., Strong, light, multifunctional fibers of carbon nanotubes with ultrahigh conductivity, *Science* 339 (6116) (2013) 182–186.
- [54] O. Hjortstam, P. Isberg, S. Söderholm, H. Dai, Can we achieve ultra-low resistivity in carbon nanotube-based metal composites? *Appl. Phys. A* 78 (8) (2004) 1175–1179.
- [55] D.B. Butrymowicz, J.R. Manning, M.E. Read, Diffusion in copper and copper alloys. Part I. Volume and surface self-diffusion in copper, *J. Phys. Chem. Ref. Data* 2 (3) (1973) 643–656.
- [56] J.R. Lloyd, J. Clemens, R. Snede, Copper metallization reliability, *Microelectron. Reliab.* 39 (11) (1999) 1595–1602.
- [57] Q. Huang, C.M. Lilley, R. Divan, An in situ investigation of electromigration in Cu nanowires, *Nanotechnology* 20 (7) (2009), 075706.
- [58] J.R. Lloyd, Electromigration failure, *J. Appl. Phys.* 69 (11) (1991) 7601–7604.
- [59] M. Raghunath, Y. Yinxiang, B. Kevin, B. Thomas, D.M. James, Breakdown current density of graphene nanoribbons, *Appl. Phys. Lett.* 94 (6) (2009), 243114.
- [60] M. Umesh, A. Sundaresan, U.K. Giridhar, Graphene–Ni(111) synergy influencing crystalline orientation, grain morphology and magnetic properties of poly-Ni, *J. Phys. Chem. C* 122 (25) (2018) 13962–13968.
- [61] M. Umesh, K. Narendra, R. Dhanya, N. Chandrabhas, U.K. Giridhar, Low cost, rapid synthesis of graphene on Ni: an efficient barrier for corrosion and thermal oxidation, *Carbon* 78 (11) (2014) 384–391.
- [62] W.H. Preece, On the heating effects of electric currents, *Proc. Roy. Soc. Lond.* 44 (36) (1988) 109–111.
- [63] C.L. Liu, Screening beneficial dopants to Cu interconnects by modeling, *Appl. Phys. Lett.* 80 (5) (2002) 763–765.
- [64] M. Shatzkes, J.R. Lloyd, A model for conductor failure considering diffusion concurrently with electromigration resulting in a current exponent of 2, *J. Appl. Phys.* 59 (11) (1998) 3890–3893.
- [65] Y. Chai, P.C.H. Chan, Y. Fu, Y.C. Chuang, C.Y. Liu, Copper/carbon nanotube composite interconnect for enhanced electromigration resistance, in: *Proc 58th Electronic and Components Technology Conf. Lake Buena Vista (Florida, USA)*, 2008, pp. 412–420.
- [66] M. Ohring, *Reliability and failure of electronic materials and devices*, Academic Press 234 (4774) (2014) 340–345.